communications engineering

Article

A Nature Portfolio journal

https://doi.org/10.1038/s44172-025-00542-y

Thermomagnetic generators for ultra-low-grade marine thermal energy harvesting

Erick Moreno Resendiz, Tavis Peterson & Ravi Anant Kishore

Low-grade thermal gradients in marine environments represent an underexploited energy source for autonomous sensing and monitoring. Converting such small temperature differences into usable electrical power remains a key challenge for ocean-deployed systems. We present a deployable thermomagnetic generator thoroughly characterized for marine-relevant energy harvesting. The device powers an internet-connected sensor and harvests ultra-low temperature differences akin to those at the ocean surface. It draws heat from water and rejects it to ambient air, operating optimally at a temperature difference (ΔT) of ~7.5 °C. Laboratory prototypes generated up to 6.7 mW at ΔT ~ 10 °C with gentle airflow (~1 m s^{-1}). A separate controlled wave-tank demonstration validated stable operation and sensor powering under marine-like boundary conditions. Given its voltage and power margins, the generator could sustain multiple sensor nodes. Scalability and material assessments identify modular deployment and non-rare-earth alternatives as pathways toward practical marine energy harvesting and low-grade waste-heat recovery.

Low-grade natural heat, such as solar, geothermal, and marine energy, is ubiquitous. Additionally, the inherent inefficiency in energy conversion processes results in a substantial portion of input energy being transformed into waste heat. Only ~28% of the total global primary energy is effectively converted into a usable form, while the remaining 72% is lost and released into the atmosphere and seas, mostly in the form of low-grade waste heat (<100 °C)[1,2]. This substantial wasted heat not only lowers energy conversion efficiency but also contributes to the ongoing issue of global warming[3–5]. Repurposing low-grade heat into a usable form, such as mechanical and/or electrical energy, is a challenge, as the conventional thermal energy conversion technologies, such as the steam Rankine cycle, cannot be effectively applied under such a low operating temperature condition. In response, various innovative technologies implementing the organic Rankine cycle[6,7], the Kalina cycle[8,9], the Seebeck (thermoelectric) effect[10], the thermoacoustic effect[11], and the pyroelectric effect[12] have been pursued.

Among the many environments where low-grade heat is abundant, the ocean is particularly compelling. Oceans continuously exchange heat with the atmosphere, creating persistent but modest temperature gradients that remain largely untapped. At the same time, maritime activities increasingly depend on distributed power for sensors, navigation aids, and communication systems far from shore. Despite remarkable advances in sensing and power electronics, <20% of the oceans have been explored or mapped[13]. Two factors account for this gap: the vast scale of the ocean itself and the power requirements of observation systems, which are constrained by limited battery capacity and data transmission demands. Ocean observation often requires only milliwatt- to watt-scale power, but the critical need is for a continuous and reliable supply over long durations in harsh marine conditions.

This urgency has been formally recognized in the U.S. Department of Energy's Powering the Blue Economy™ report, which highlights ocean observation and navigation as a promising near-term market[14]. Most deployed maritime sensors and navigation aids today are either tethered to onshore power or rely on local battery storage with finite lifespans[15,16]. Their remoteness, combined with growing demand for wireless data telemetry, underscores the pressing need for resilient, self-sustaining marine energy solutions capable of powering a range of scientific, military, and commercial activities. While solar, wave, and wind energy are often used to power ocean sensors, their intermittency and dependence on local conditions make them unreliable for autonomous, long-term operation. Thus, the availability of underutilized thermal gradients in the ocean represents a unique and underexplored opportunity for sustainable power generation.

In this context, this study explores the potential of thermomagnetic generators as a compact and adaptable approach to harvesting ultra-low-grade heat. By leveraging naturally available temperature gradients between the top ocean surface and ambient air, thermomagnetic generators can provide a reliable, independent, and continuous power source for distributed marine sensors, expanding the scope of autonomous ocean exploration.

Thermomagnetic generators are broadly classified into two categories: active thermomagnetic generators and passive thermomagnetic generators. Active thermomagnetic generators directly convert the magnetic transition into electrical power generation using the electromagnetic effect. In its

National Renewable Energy Laboratory, Golden, CO, USA. e-mail: Ravi.Kishore@nrel.gov

simplest form, this phenomenon is typically achieved by utilizing a C-shaped permanent or electromagnet, with a ferromagnetic material placed as a shunt between the magnet's poles and a winding (coil) around the shunt material. The ferromagnetic material is cyclically heated and cooled, causing a varying magnetic flux that induces an electromotive force within the coil through Faraday's law of electromagnetic induction. Although active thermomagnetic generators theoretically offer higher efficiency by avoiding intermediate conversion steps, experimental efficiency is often limited by unsatisfactory material properties, device design, and the need for circulating the thermal fluids. Passive thermomagnetic generators, also referred to as thermomagnetic motors or Curie motors, convert thermomagnetic energy into mechanical energy, e.g., linear or rotary motion, which is eventually used for electricity generation. These devices typically comprise a ferromagnet placed in the presence of a permanent magnet. A spacious thermal gradient (i.e., the temperature difference between a heat source and a heat sink) is typically used to convert thermal energy into mechanical energy in the form of rotary or linear motion. When the temperature across the ferromagnet is uniform, its magnetic permeability is also uniform and is subjected to the applied magnetic field, and the thermomagnetic generator establishes a mechanical equilibrium where magnetic forces are balanced. However, when a portion of the ferromagnet is heated above its Curie temperature using a heat source, thermal equilibrium is disrupted, thereby altering the magnetic permeability, and unbalanced magnetic forces are generated, causing motion. With cyclic disruption in the thermal equilibrium of the ferromagnet due to the presence of a continuous heat source and a heat sink, mechanical work is produced. Subsequently, an electromechanical or electromagnetic device is coupled to effectively transform the motion into electricity. Further information regarding the thermomagnetic cycle and the corresponding system configuration can be found in Supplementary Note 1, including Supplementary Figs. 1 and 2.

Despite the relatively low current and output power, passive thermomagnetic generators are particularly attractive due to their simplicity and adaptability for integration with existing energy systems, such as photovoltaic panels, data servers, and thermal reservoirs like oceans and geothermal sources that are warmer than the ambient air. Considering these factors, we have used this configuration for the thermomagnetic generator design presented in this paper for marine thermal energy harvesting.

The literature related to passive thermomagnetic generators reflects a dynamic and growing field, addressing the transformative capacity of these systems to address the exploitation of low-grade heat.

- The concept of the thermomagnetic motor dates back to 1889, documented in US Patent 396121[17], which proposed using temperature-dependent magnetic properties to drive mechanical motion and laid the groundwork for later developments.
- A practical thermomagnetic motor was demonstrated in the 1970s, showing feasibility for thermal conversion and heat recovery despite material limitations at the time[18].
- Disc- and cylindrical-type thermomagnetic motors with equal working material volume were compared; the disc configuration delivered higher power and torque due to reduced eddy-current braking, despite added water friction. This supports allocating additional volume radially (increasing rotor diameter) rather than axially (thickness)[19].
- A review of thermomagnetic materials and device architectures identified gadolinium (Gd) as a favorable working material owing to its second-order magnetic transition and near-room-temperature Curie point, which together enable higher thermomagnetic efficiency and make it well suited for low-grade heat conversion[20].
- A survey of thermomagnetic harvesters delineated active versus passive architectures; while passive devices offer lower conversion efficiency than active systems, they remain useful as actuators and for augmenting heat rejection of hot bodies[21].
- A single-rotor thermomagnetic motor using Gd demonstrated that performance depends critically on maintaining a strong, uniform magnetic field aligned with the direction of rotation, which provides the advancing force; this requirement is best met by a solenoidal-like field[22].
- A Gd-based thermomagnetic motor was modeled with water-driven forced convection for heating and cooling; a parametric study indicated performance degradation when the hot-side temperature exceeded 65 °C and showed that maximum torque depends sensitively on permanent magnet placement, motivating an optimized layout[23].
- A Gd-based thermomagnetic motor with doubled heating/cooling zones and magnet count showed less improvement than expected: inefficient heat transfer prevented full rotor cooling before re-entering the magnet region, an effect linked to lower relative magnetic permeability[24].
- A thermomagnetic motor using Mn_2FeSn as the working material showed, via Multiphysics analysis, that radial (diametral) rotor thickness is the dominant lever on output when heat transfer is well managed; performance further improves with higher cooling rates, especially when cooling and heating rates are matched[25].
- Heat-transfer analysis with water (heating) and air (cooling) jet impingement showed that performance is primarily limited by the cooling side: due to air's inferior thermophysical properties, substantially higher airflow is required to match the effectiveness of water[26].
- An experimental parametric study on a miniature thermomagnetic generator with continuous Gd rings as rotors showed that partial immersion in hot water, with the ambient environment serving as a heat sink, provides a simpler alternative to forced convection cooling/heating employed in earlier designs[27].

To date, most of the studies related to thermomagnetic generators employed forced convection as the heat transfer method[19,22–26], which makes the system complex and limits its implementation in real-world applications where natural or waste heat (e.g., warm/cold water source) is naturally available. Additionally, the energetic expenditure to drive the thermal fluids often surpasses the energy recovered by the thermomagnetic generators due to their low energy conversion efficiency under a small thermal gradient. A subsequent design demonstrated partial immersion with ambient heat sinking as a simpler, more versatile approach suited to practical settings[27]; however, that early concept still left substantial headroom for improvements in performance and deployability.

The present study advances technology by introducing an improved and application-specific generator for repurposing waste and naturally occurring low-grade heat to power wireless sensors, with a particular focus on marine thermal energy. In addition to targeting observation sensors with typical power demands of 0.5–5.0 mW, which are critical for tracking ocean environments[28,29], this work explores key design parameters, including immersion angle, shaft thickness, and rotor spacing, which are essential for optimizing performance and material utilization. A case study incorporating realistic oceanographic data is used to define viable deployment conditions, and experimental validation in a controlled water wave tank bridges the gap between laboratory design and marine application. Finally, the study introduces a discussion of scalability and design strategies informed by this analysis, including modular deployment pathways and alternative material approaches, establishing a clear trajectory toward practical, low-power energy harvesting for marine monitoring.

Results and discussion

Working material, principle, and design

Material selection. The thermomagnetic generator employs Gd as the working material. Gd has a Curie point of about 20 °C[30], which is the temperature at which the ferromagnetic-to-paramagnetic phase transition happens; thus, it is directly related to the operation and energy

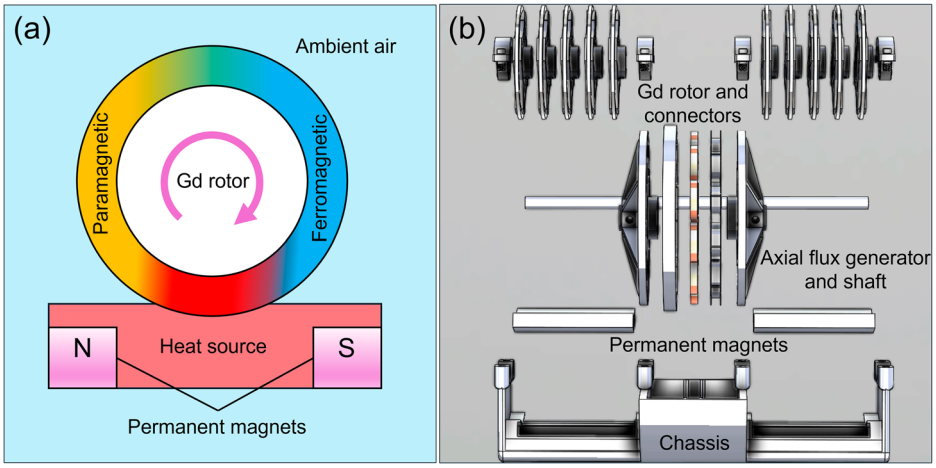

Fig. 1 | Thermomagnetic generator. a Operating principle; **b** scalable design.

conversion efficiency of thermomagnetic devices. Compared to many other ferromagnetic material options for applications near-room temperature[25], Gd exhibits a higher magnetization change, leading to a higher magnetic work output[20]. Additionally, Gd exhibits a relatively lower specific heat of ~280 J kg^{-1} K^{-1} and better thermal conductivity of ~9 W m^{-1} K^{-1}. These thermal characteristics result in high thermal diffusivity and thus better thermal transport, indicating a rapid thermal cycling[31]. Lastly, Gd undergoes a second-order magnetic phase change and exhibits minimal thermal hysteresis, which is crucial to obtain continuous magnetic work from a thermomagnetic cycling process[21].

Operating principle. The working principle of the thermomagnetic generator is broadly the same as what was reported in our previous research[27]. The thermomagnetic generator consists of three key components: ring-shaped Gd rotors, permanent magnets, and an axial flux generator. Warm liquid (e.g., water) at a temperature of ~25–40 °C heats a small section of the ferromagnetic rotors, as shown in Fig. 1a. The external magnetic field is created by the permanent magnets located below these rotors. The portion of the rotor in contact with the heat source gains heat, reaches a temperature above the Curie point, and undergoes the ferromagnetic-to-paramagnetic phase transformation. This process drastically reduces the magnetic interaction between the hot portion of the rotor and the permanent magnets. Because the remaining section of the rotor is still cold and in the ferromagnetic phase, the permanent magnet attracts the cooler portion, causing the rotor to rotate. An axial flux generator converts rotational energy into electricity.

Scalable design. Our thermomagnetic generator has been designed as a scalable device, as shown in Fig. 1b. An axial flux generator is connected to a long central shaft that can hold multiple Gd rotors. Large permanent magnets are inserted into a chassis on both sides, with smaller permanent magnets placed on top of the larger ones to concentrate and enhance the magnetic field flux. The axial flux generator was designed and fabricated in such a way that it minimizes frictional losses and the starting torque, experiences minimal stray magnetic field, and produces an output DC voltage greater than 3.0 V, which is essential for powering most Internet of Things (IoT) sensors. More details related to the axial flux generator are provided in the Experimental Procedures section and in the Supplementary Methods. All the Gd rotors have an outer diameter of 2.0 inches (50.8 mm), an inner diameter of 1.75 inches (44.5 mm), and a thickness of 0.06 inch (1.5 mm). The Gd rotors are concentrically connected to the axial flux generator through a 0.25-inch (6.35 mm) non-magnetic shaft. Lastly, all the components are assembled into a 3D-printed polycarbonate chassis using ball bearings, non-magnetic fasteners, and structural adhesive or epoxy.

Performance characterization

The performance characterization of the thermomagnetic generator is a comprehensive analysis of various parameters and their effect on the voltage and power output under various operational conditions.

Immersion angle. The immersion angle (θ) serves as a crucial parameter, delineating the depth to which the Gd rotor is immersed in water and, consequently, influencing the heat transfer during the heating cycle. Although higher immersion (i.e., greater θ) provides a larger area for heat transfer, it increases the drag on the rotor as it rotates in the water. To investigate the impact of the immersion angle, a series of experiments was conducted using a pair of Gd rotors, with one rotor positioned on each side and the axial flux generator with no load attached. The experiments (Fig. 2) revealed nearly a linear correlation between the immersion angle and the rotor's angular speed when θ is greater than an optimal value. At the tested water temperature (T_{water} = 30 °C), the optimal immersion angle ($\theta_{optimal} \approx 21°$) balances heat transfer and drag on the Gd rings, facilitating efficient heat removal while minimizing drag. When θ is less than $\theta_{optimal}$, it results in an unstable meniscus region, causing a dramatic decrease in heat transfer between the water and the Gd rotor, which disrupts the heating and cooling cycle, thereby lowering angular speed. Conversely, if θ exceeds $\theta_{optimal}$, the overheated Gd portion must slow down to maintain the necessary heat transfer, resulting in decreased performance. To optimize the immersion angle from a practical standpoint, it is essential to implement precise manufacturing and assembly processes so that all the rotors are equally immersed. This process ensures uniform wetting and stability of the meniscus at high T_{water}, which is crucial for effectively balancing heat transfer. Additionally, the inherent poor thermal properties of air (lower density, thermal conductivity, and specific heat) compared to those of water require a larger cooling area compared to the heating zone to balance the heat transfer rate. The value of $\theta_{optimal}$ was found to decrease at high T_{water}, emphasizing the fact that cooling is currently the key limiting factor for these devices.

Axial generator air gap distance. Given that the magnetic flux density decreases with the square of the distance, the efficiency of an axial flux generator is inversely related to the air gap raised to the fourth power. Therefore, it is crucial to minimize the air gap without compromising manufacturability and assembly. The air gap distance was adjusted by placing a 1.5 mm thick non-magnetic washer between the electric rotors; see Supplementary Methods for more information.

The results from Fig. 3 illustrate the performance across three different air gaps. As shown in Fig. 3a, a 6.8 mm gap produced 2.28 mW, an 8.3 mm gap yielded 2.04 mW, and a 9.8 mm gap generated 1.80 mW. These results correspond to power reductions of 10.5% and 20.8% relative to the 6.8 mm gap. Notably, the power decay appeared to follow a similar trend to the

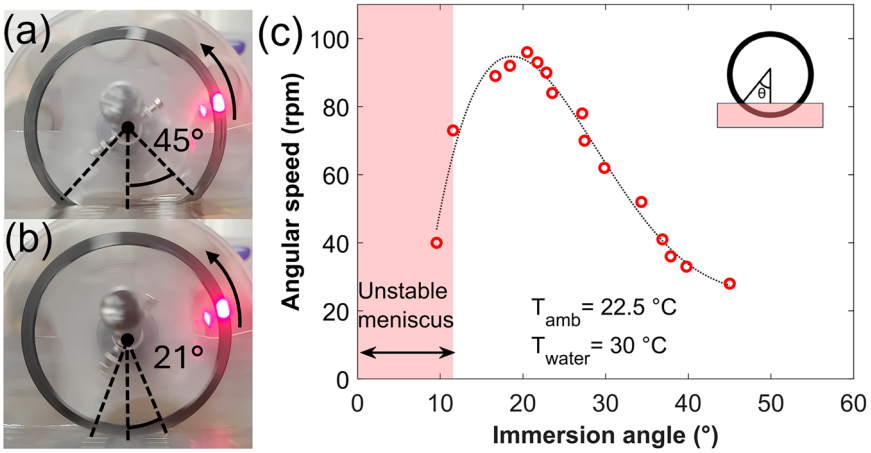

Fig. 2 | Effect of the immersion angle on the performance of the thermomagnetic generator. Images illustrating: **a** a high immersion angle, **b** optimal immersion, and **c** Immersion angle versus the rotors' angular speed at the no-load condition. A fourth-order polynomial least-squares fit was used to generate the fitting curve shown in panel (c).

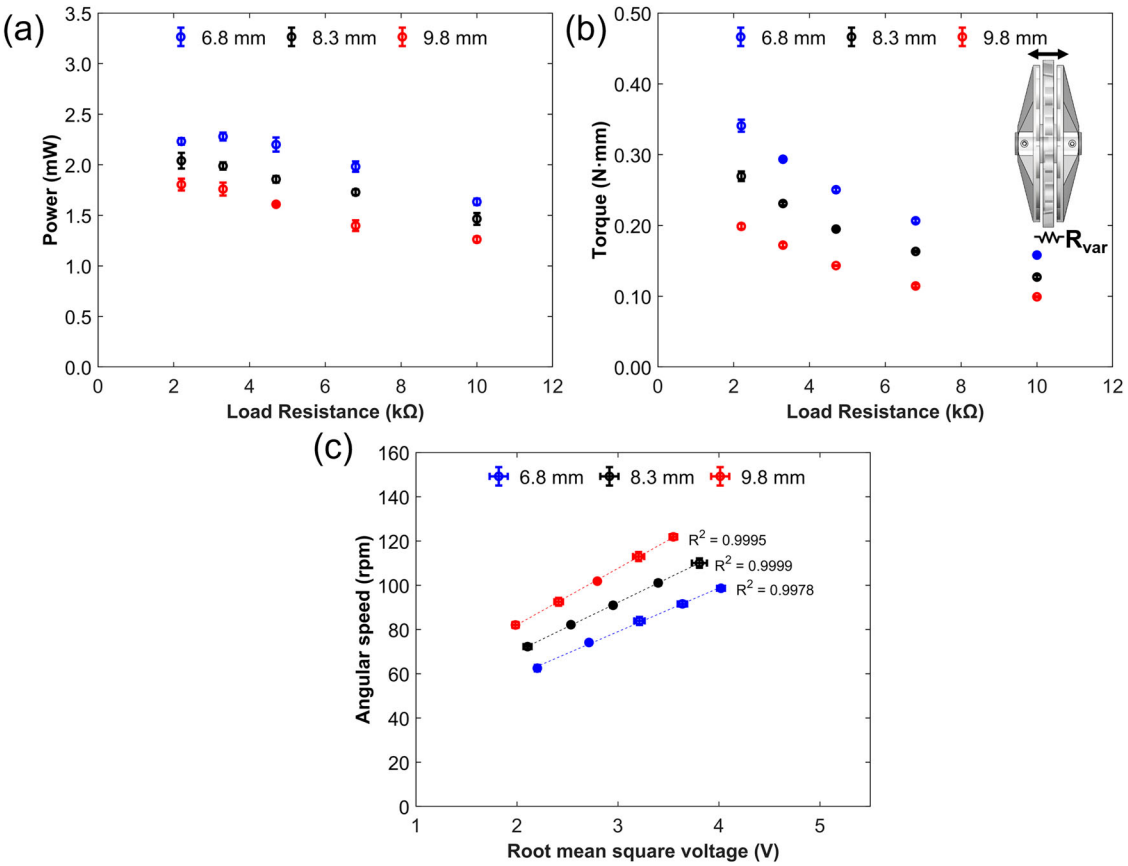

Fig. 3 | The experimental study on the impact of the axial flux generator air gap distance on the performance of the thermomagnetic generator. a Power output and **b** torque versus load resistance. **c** Angular speed versus root mean square voltage. The water and air temperatures were ~30.0 °C and ~22.5 °C, respectively, for all experiments. The error bar was calculated using the standard deviation method of the experimental data.

average magnetic field flux at the air gap, which decreased by 10.44% and 19.68% as computed using COMSOL. Regarding torque, Fig. 3b indicates that the different air gaps produced the following values: 0.34 N-mm for the 6.8 mm gap, 0.269 N-mm for the 8.3 mm gap (a reduction of 20.9%), and 0.198 N-mm for the 9.8 mm gap (a reduction of 41.6%). When comparing the torque reduction to the increase in the air gap, a linear inverse relationship is observed for the tested air gaps. Specifically, an increase in the air gap of 22.05% and 44.1% resulted in a torque reduction of 20.9% and 41.6%, respectively. Figure 3c illustrates a nearly perfect linear relationship between angular speed and root mean square (RMS) voltage. As the air gap distance increases, the slope increases, indicating that a higher angular speed is required to achieve the same RMS voltage. This trend underscores the decay in performance associated with larger air gaps in the axial flux generator.

The selected air gap distances of 6.8 mm, 8.3 mm, and 9.8 mm were not arbitrary; rather, they were constrained by practical design considerations. The lower limit was defined by the physical thickness of the stator, which ensured mechanical clearance and prevented any interference or collision during rotation. The upper limit was set by the maximum allowable distance within the axial flux generator enclosure (see Fig. 1).

It was found that the 9.8 mm air gap produced sufficient energy to power a wireless sensor, which was a crucial part of this study. However, the assembly and experimentation were not easier compared to the 8.3 mm air

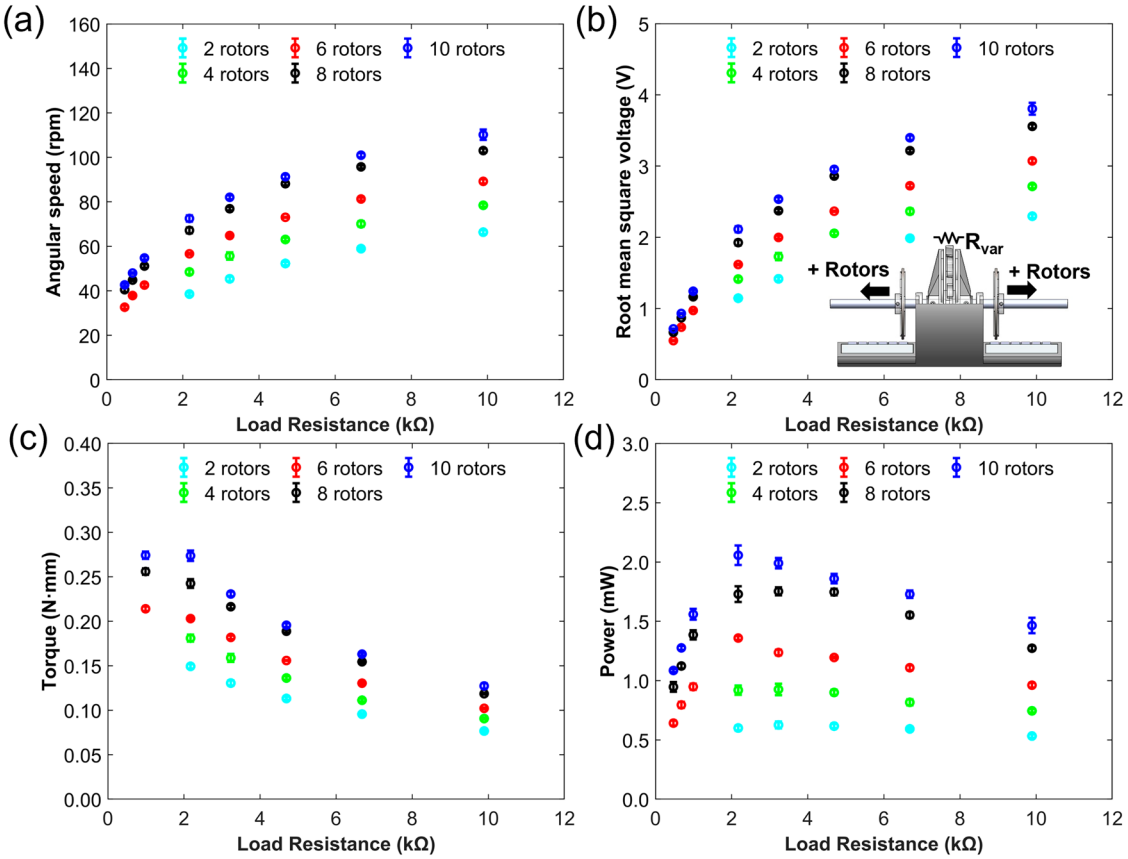

Fig. 4 | The experimental study on the impact of the number of rotors on the performance of the thermomagnetic generator. a Angular speed, **b** root mean square voltage, **c** torque, and **d** power output. The water and air temperatures were ~30.0 °C and ~22.5 °C, respectively, for all experiments. The error bar was calculated using the standard deviation method of the experimental data.

gap. In contrast, the experimentation with the 8.3 mm air gap was considerably easier than the 6.8 mm air gap, primarily due to irregularities in the chassis interfering with the electric rotors. As a result, the 8.3 mm air gap was selected for all the experiments in this study.

Number of rotors. The number of rotors of the thermomagnetic generator is directly proportional to the volume of thermomagnetic materials; therefore, as the number of rotors increases, so does the magnetic force, resulting in higher torque under the influence of an external magnetic field. A higher torque under a constant resistive load condition translates directly into an increased generated power. A higher number of rotors, however, can increase frictional losses and drag forces that have negative effects on the generator's performance. Additionally, a mismatch between the magnetic torque due to an increased rotor count and the rated design parameters for the axial flux generator would result in lower-energy conversion efficiency. Therefore, assessing the impact of the number of rotors on the generator's performance is critical to explore the scalability possibilities of the thermomagnetic power generation technology.

Figure 4 depicts a comprehensive experimental characterization of the thermomagnetic generator as the number of Gd rotors is increased. Figure 4a shows that the angular speed increases with both an increase in the number of rotors and an increase in the resistive load. Increasing the number of rotors causes increased angular speed due to higher magnetic torque; however, due to increased frictional losses and air/water-related drag, there are diminishing returns. On the other hand, increasing the resistive load lowers the electric current flow in the axial flux generator and thus lowers the back electromotive force, thereby resulting in a higher angular speed of the thermomagnetic generator. More specifically, the average angular speed observed at a resistive load of 10 kΩ was about 66 rpm for 2 rotors, which increased to ~78 rpm for 4 rotors, ~89 rpm for 6 rotors, ~103 rpm for 8 rotors, and ~110 rpm for 10 rotors.

Faraday's law of electromagnetic induction establishes a direct proportionality between the electromotive force and angular speed, determined by the rate of change in magnetic flux. Consequently, the angular speed and the RMS voltage follow the same trend (Fig. 4b). The RMS voltage increases with the increase in both resistive load as well as the number of rotors; however, we note diminishing returns. An axial flux generator's current reaches its maximum when the angular speed—and, consequently, the voltage—approaches zero. Conversely, the voltage output is maximum when the angular speed is highest and the current is zero (i.e., the circuit is open). At a resistive load of 10 kΩ, we note an RMS voltage (V_{RMS}) of 2.29 V for 2 rotors, 2.71 V for 4 rotors, 3.07 V for 6 rotors, 3.55 V for 8 rotors, and 3.80 V for 10 rotors.

Notably, as depicted in Fig. 4c, the torque, being directly proportional to the current, also approaches its maximum under these conditions. Lastly, as illustrated in Fig. 4d, maximum power outputs of 2.05 mW, 1.73 mW, 1.35 mW, 0.92 mW, and 0.6 mW were achieved with 10-, 8-, 6-, 4-, and 2-rotor configurations, respectively, at the optimal resistive load of ~2.2 kΩ.

While the power output of the thermomagnetic generator increases with the increase in the number of rotors, we note diminishing returns, which results in a concurrent decrease in power density. Figure 5 depicts the power output per unit rotor of the thermomagnetic generator. The power per unit rotor varies from 0.30 mW for the generator with 2 rotors to 0.205 mW for the generator with 10 rotors. Although the decrease in power is gradual, we note that the power per unit rotor begins to plateau beyond 4 rotors, stabilizing near 0.23 mW. The observed saturation in power per rotor is primarily attributed to cumulative effects such as magnetic interaction,

uneven immersion angles, and non-uniform wetting, which lead to increasingly asymmetric thermal cycles as more rotors are added. In contrast, the main sources of experimental uncertainty, including slight variations in immersion angle and local temperature, are present across all configurations but remain relatively small in magnitude. As the number of rotors increases, however, the compounded impact of magnetic and thermal interactions grows, ultimately limiting performance gains and resulting in the plateau observed beyond four rotors. Despite minor fluctuations between configurations, such as those between the 4- and 6-rotor cases, the underlying trend remains consistent and highlights the physical limitations governing scalability in the system.

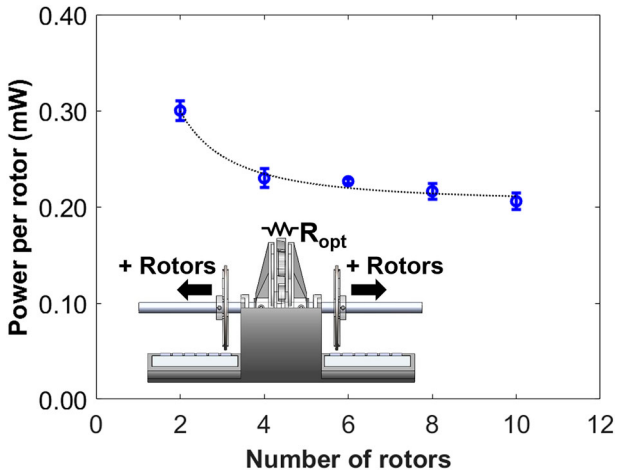

Fig. 5 | The maximum power output per unit rotor of the thermomagnetic generator as a function of the number of rotors. The water and air temperatures were ~30.0 °C and ~22.5 °C, respectively, for all experiments. The error bar was calculated using the standard deviation method of the experimental data.

Shaft effect. Analyzing the shaft of the thermomagnetic generator is crucial to ensure its structural integrity and performance reliability. This analysis contributes to enhancing the understanding and optimization of the mechanical components, ultimately leading to improved efficiency and durability. A large-diameter, solid shaft allows for tighter machining tolerances and reduces deformations under continuous downward magnetic force; however, it may also introduce a more massive design with increased inertia that may negatively affect the generator's performance. Figure 6 illustrates the torque and power output of the thermomagnetic generator using three different 303 stainless-steel off-the-shelf shafts: a 0.125-inch (3.175 mm) solid shaft, a 0.250 inch (6.35 mm) solid shaft, and a 0.250 inch (6.35 mm) hollow tube. Although the results depict some differences, the performance remains comparable and within experimental variability. This observation suggests that, at this scale, the mass of the shaft is negligible and changes in shaft dimensions would not exert a substantial effect on the moment of inertia of the entire rotor structure.

Rotor spacing. The compactness of the device is inherently influenced by the rotor spacing, making it a critical parameter to consider. Although a smaller spacing between the rotors makes the device compact, it can negatively affect the heat transfer between the rotor and the ambient air. Achieving the right rotor spacing is essential for avoiding unnecessary

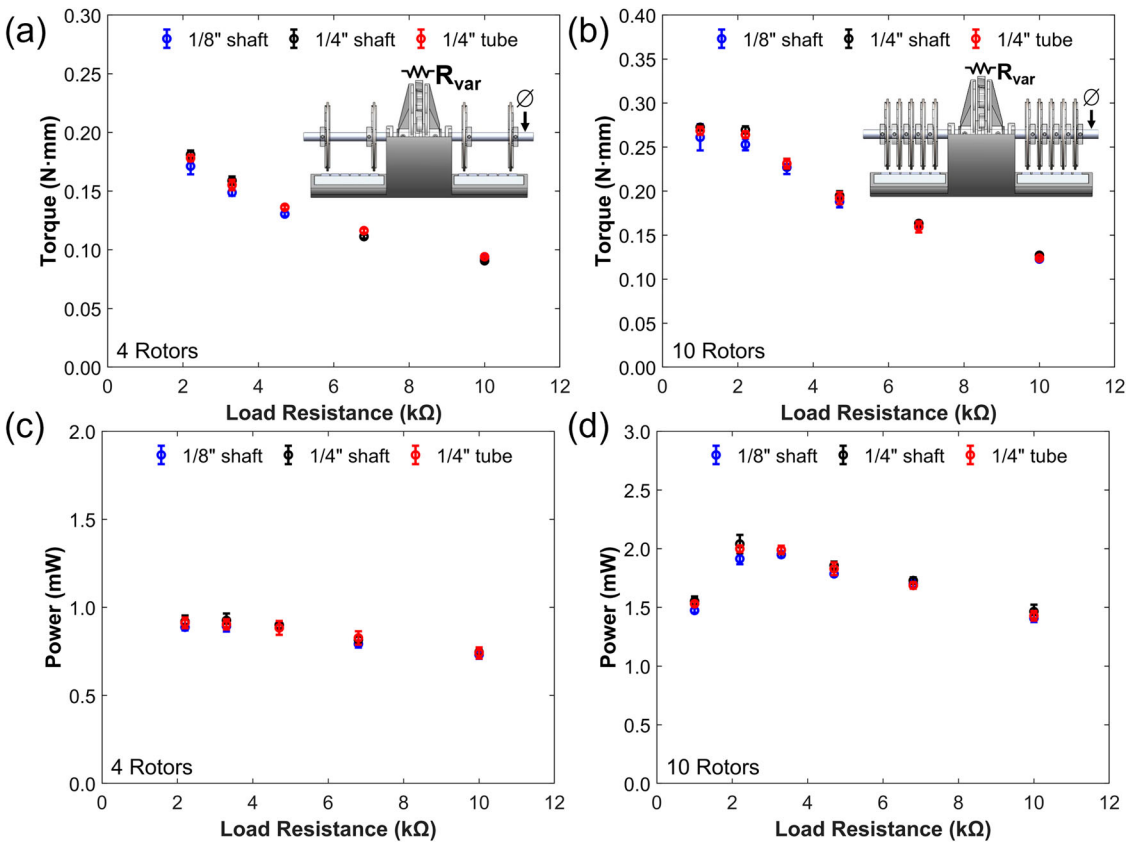

Fig. 6 | The effect of shaft diameter on the thermomagnetic generator performance. a Torque versus load resistance for the generator with four rotors. **b** Torque versus load resistance for the generator with 10 rotors. **c** Power versus load resistance for the generator with four rotors. **d** Power versus load resistance for the generator with 10 rotors. Water and air temperatures are ~30.0 °C and ~22.5 °C, respectively, for all experiments. The error bar was calculated using the standard deviation method of the experimental data.

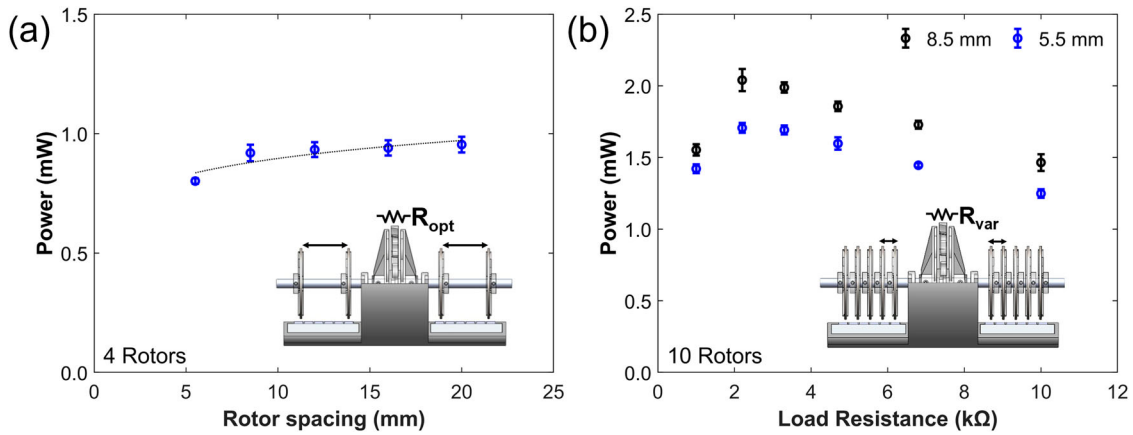

Fig. 7 | The impact of rotor spacing on the performance of the thermomagnetic generator. a 4 rotors and **b** 10 rotors. **a** Maximum power output versus rotor spacing. **b** Power output versus load resistance. The water and air temperatures are ~30.0 °C and ~22.5 °C, respectively, for all experiments. The error bar was calculated using the standard deviation method of the experimental data.

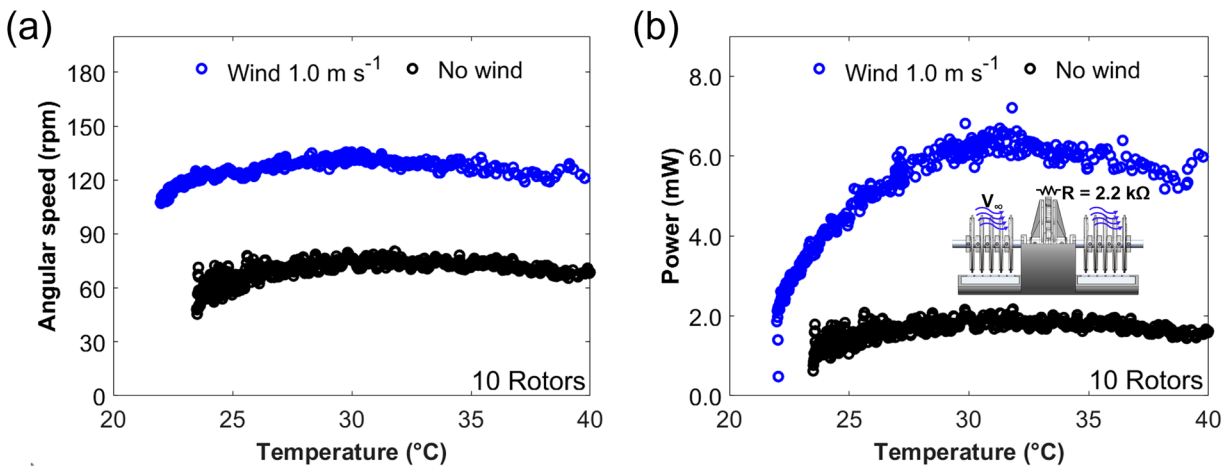

Fig. 8 | Operation of the thermomagnetic generator under no wind and a wind speed of 1 ms^{-1}. a Angular speed versus water temperature. **b** Power output versus water temperature. Ambient air temperature is ~22.5 °C.

volume increase while ensuring that the gap is not too small as to hinder the generator's performance.

Figure 7 sheds light on the impact of reducing rotor spacing on the power generation. The closer the rotors are, the more intricate the interplay of magnetic, heat transfer, and fluid dynamics that exists between them. These insights highlight the nuanced relationship between the rotor spacing and the generator's performance, emphasizing the need for careful optimization in achieving peak device performance. The 4- and 10-rotor configurations are intentionally selected to study the impact of minimum and maximum possible rotor spacing under the fixed chassis size of the thermomagnetic generator.

In Fig. 7a, it becomes evident that a smaller gap results in a lower maximum power output. To achieve higher performance, optimal rotor placement is essential, minimizing interference between the rotors. However, this pursuit may necessitate a larger device, compromising the power density per footprint. This issue underscores the necessity for more effective heat transfer, a factor limited in the compact configuration compared to the spaced one.

Wind effect. Analyzing how the thermomagnetic generators perform under wind versus no-wind conditions is important to estimate the generator's performance under outdoor conditions. Although precise-airflow-related experiments require a wind tunnel, here we use an axial-flow box fan to recreate a chaotic, windy outdoor condition near the ground, where wind is typically slow, non-uniform, and gusty. The box fan was located at a certain distance from the thermomagnetic generator, and the wind speed was measured using an anemometer. All the measurements were performed when the anemometer showed a wind speed of 1.0 m s^{-1}.

Figure 8 compares the angular speed and power produced by the thermomagnetic generator with 10 rotors when there is no wind and when there is wind. The experiment starts with the thermomagnetic generator resting at the normal ambient temperature. The water was gradually heated, and the generator's angular speed and power output were measured as the water temperature increased over time.

Figure 8a shows the generator's angular speed versus water temperature. Under no wind, the thermomagnetic rotors achieve angular speeds ranging from ~40 to 80 rpm, initiating rotation at ~24 °C. As the water temperature increases, the angular speed rises, peaking between 29 °C and 31 °C. However, beyond this peak, the angular speed gradually decreases due to excessive heat accumulation in the thermomagnetic rotors. In contrast, when wind is present at 1 m s^{-1}, the generator exhibits a peak angular speed of up to 135 rpm and begins rotation at a lower water temperature of ~22 °C, slightly below the ambient air temperature of 22.5 °C.

The power output of the generator is closely related to the water temperature, as illustrated in Fig. 8b. Under no-wind conditions, the generator's power, measured at the resistive load of 2.2 kΩ, varies between

1.5 mW and 2.13 mW, peaking at water temperatures of 29–31 °C, which aligns with the peak angular speed. In the presence of wind at approximately 1 m s^{-1}, power output increases, reaching between 5.5 mW and 6.7 mW at water temperatures of 31–33 °C. This substantial enhancement highlights the critical role of cooling in the thermomagnetic cycle: the strong response to forced convection confirms that heat rejection, rather than heating, is the primary limiting factor in the generator's operation. The wind not only improves convective and evaporative cooling, allowing higher sustained operating temperatures, but also enables effective performance even slightly below ambient air temperature.

Power in context. In still air, the thermomagnetic generator delivers 2.05 mW (15 μW cm^{-2}) at room temperature (T_{hot} ~ 30.0 °C, T_{cold} ~ 22.5 °C; ΔT = 7.5 K). Under a gentle 1 m s^{-1} wind speed, the power output reaches 6.7 mW (46 μW cm^{-2}) at the same heat source and sink temperatures. For reference, the state-of-the-art thermoelectric generators (TEGs) at ΔT ~ 10–15 K in still air conditions typically yield a power density of 4.5–18.4 μW cm^{-2} [32–35]. Under light wind speed of 2–3 m s^{-1} and ΔT ~ 15–20 K, the reported power density for TEGs is 45.6–71.8 μW cm^{-2} [33,36]. Achieving 15–46 μW cm^{-2} at smaller ΔT (< 7.5 K) and lower wind (~ 1 m s^{-1}) underscores the thermomagnetic generators' capability for operation in ultra-low-grade, ambient thermal environments. More specifically, a study on TEG reported 4.5 μW cm^{-2} at T_{hot} ~ 32.0 °C and T_{cold} ~ 22.0 °C (ΔT = 10 K)[35]. In comparison, our device delivers ~3.3× higher power density under nearly identical conditions. Additionally, the output voltage of the thermomagnetic generator is several volts that are appropriate for the IoT sensors, whereas TEG at a small temperature difference generates micro-to-milli-volts and thus requires a voltage booster for energy harvesting applications. Other energy harvesters such as wind- and wave-driven triboelectric nanogenerator (TENG) and electromagnetic generator (EMG) are generally characterized by absolute power output (mW), with results ranging from sub-milliwatt to tens of milliwatts depending on wind speed (4–13 m s^{-1})[37–39] or wave excitation[40,41]. Although these values are not directly normalized by area, they provide a useful context for situating our devices' performance. The power values and test conditions for various kinds of low-temperature energy harvesters are compiled in Supplementary Note 2 (Supplementary Table 1).

Demonstration with IoT sensors, case study and design considerations

Energy storage. To investigate the suitability of the thermomagnetic generator for low-power energy storage applications, two storage configurations were tested using a breadboard circuit: a 3.2 V, 450 mAh $LiFePO_4$ rechargeable battery and a 0.5 F supercapacitor. The objective was to evaluate the duration required to reach a target charging voltage sufficient to operate the preselected wireless IoT sensor. Figure 9a depicts the recorded voltage for the rechargeable battery and 0.5 F supercapacitor. Both experiments start with nearly zero voltage, indicating a fully discharged state of the energy storage systems. The test started with the thermomagnetic generator operating under a water temperature of ~35 °C and an ambient air temperature of ~23 °C. A target charging voltage of 2.32 V was chosen based on the powering needs for the preselected wireless sensor, which is discussed subsequently. The supercapacitor reached the target voltage in about 50 min, whereas the rechargeable battery needed about 7 hours due to its considerably high storage capacity. These tests shed light on which of the energy storage methods would best be used for practical applications. Evidently, the supercapacitor reached the charging voltage much faster than the rechargeable battery, with a more than 6-hour difference. Therefore, we chose the supercapacitor as the energy storage option for further analysis.

Printed circuit board. The breadboard circuit that was used previously was not a long-term desirable solution for practical applications. A printed circuit board (PCB) was developed and assembled using nearly the same components as the breadboard circuit, but such that it would allow durable and secure operation. Further, a much-reduced size of the circuit would be beneficial for storing the circuit on board the thermomagnetic generator device, particularly for difficult-to-reach and remote applications. Figure 9b illustrates the key components of the PCB, including the bridge rectifier, a direct current to direct current (DC/DC) converter, and a supercapacitor. A few surrounding resistors and capacitors were used to make the DC/DC converter function properly. More specifically, the bridge rectifier was used to change the alternating current produced by the thermomagnetic generator to direct current. The DC/DC converter, i.e., an LTC3108 or LTC3108-1, then converted the voltage produced by the thermomagnetic generator to a value suitable for the sensor. The PCB was designed so that the output voltage of the DC/DC converter can be 2.35 V, 2.5 V, 3 V, 3.3 V, 3.7 V, 4.1 V, 4.5 V, and 5 V. The varied output voltages would allow for other applications that require different voltages. Finally, a 0.47 F supercapacitor was used to store the energy produced by the thermomagnetic generator.

IoT sensor. One of the desired applications we chose was to power a wireless humidity and temperature sensor using our thermomagnetic generator device. We used a SensorPush Humidity and Temperature Smart Sensor (www.sensorpush.com) that transmits the data to the user's phone every minute via Bluetooth. Initially, the sensor was believed to need 3.0 V to function, but after testing, it was found that the sensor could function at voltages as low as 2.05 V. Figure 9c–e shows the experiment setup, the supercapacitor performance, and the temperature and relative humidity data collected from the sensor. The experimental setup was relatively simple. The thermomagnetic generator resided in a warm water bath, and the temperature of the water was monitored by thermocouples and controlled to maintain a preset value using a feedback loop. Once the water reached roughly 27 °C, the thermomagnetic generator began to operate, generating an alternating current that was sent into the PCB, which output direct current and a suitable voltage for the sensor. For this experiment, the sensor was powered using a 2.35 V output option. Once the sensor received a voltage of 2.05 V, it powered on and started transmitting data to the user's phone (Fig. 9d). The sensor was plugged in at ~8:30 am and was unplugged ~3:00 pm. The six-and-a-half-hour temperature and humidity data collection can be seen in Fig. 9e. The same figure shows that the temperature slowly increases over time, whereas the humidity remains nearly constant under the laboratory conditions used for the experiments.

Projected cost. A detailed, itemized bill of materials and projected unit manufacturing cost for volume production is provided in Supplementary Note 3 (Supplementary Table 2). Under the stated bulk pricing and batch fabrication assumptions, the cost per unit is US$ 56.54. The table lists unit prices, quantities, and supplier references for all components (Gd material and ring fabrication, magnets, bearings/shaft, wire, adhesive, printed parts, and PCB) and documents the cost multipliers used (e.g., 50% of Gd material cost for ring fabrication; 100% of ASA plastic cost for printing).

Water and wave tank test. To further test the thermomagnetic generator, a 15-gallon aquarium was used to see how the thermomagnetic generator would perform while floating. This setup better replicates how the thermomagnetic generator would perform while in the ocean or larger water bodies. The aquarium was filled with 10 gallons of tap water, which was then heated to 31 °C using an aquarium heater. The temperature of the water was monitored using a temperature sensor that was attached to the glass of the aquarium. An overfloating structure with removable counterweights was assembled to ensure a proper θ capable of powering the wireless sensor. A new polycarbonate case surrounding the generator was constructed as well. This version encased the generator portion of the thermomagnetic generator, helping keep the generator and other electronics dry. The thermomagnetic generator with 10 Gd rings

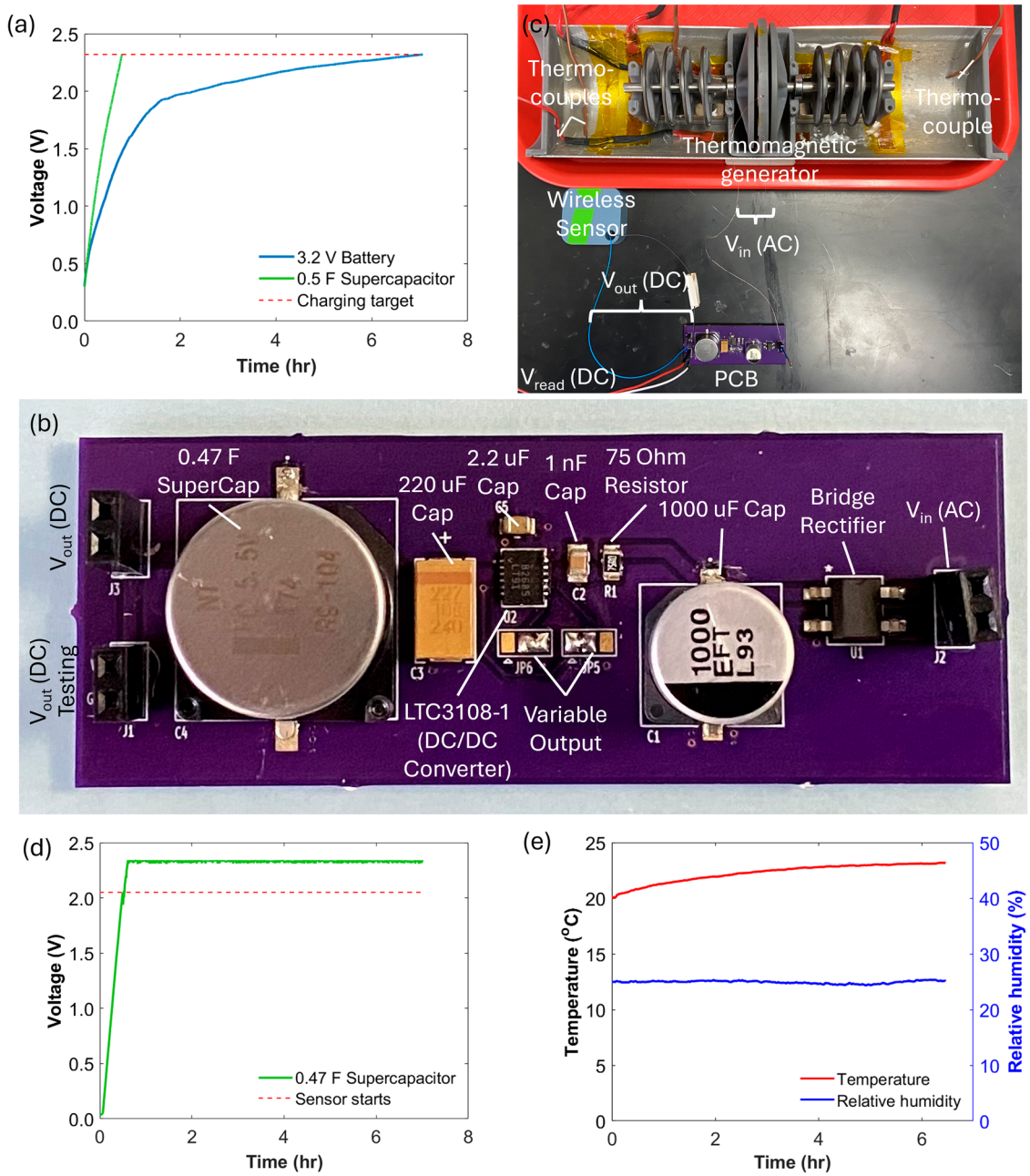

Fig. 9 | Practical demonstrations. a Electrical energy storage in a supercapacitor and a rechargeable battery. **b** Printed circuit board (PCB) designed for powering an IoT sensor. **c** Experimental setup illustrating the PCB and sensor arrangement. **d** Voltage profile in a 0.47 F supercapacitor powering a wireless temperature and humidity sensor. **e** Temperature and relative humidity data were recorded for about a 7-hour period.

reached the supercapacitor's target voltage of 2.35 V in about 21 mins. After this point, the sensor started transmitting information to the cellphone.

The thermomagnetic generator was also tested in a water wave tank at full physical size, with no geometric or dynamic scaling applied (see Supplementary Note 3, Supplementary Fig. 7). Consequently, the measured conditions correspond directly to the disturbance that the device would experience in the ocean if subject to motions of the same amplitude and period. The objective of the exercise was not to replicate realistic wave climates, but to expose the device to a range of repeatable vertical motions representative of mild surface agitation.

Three regular-wave and three irregular (JONSWAP) cases were generated, with peak periods (T_p) between 1.49 s and 2.19 s and significant wave heights (H_s) between 0.027 m and 0.072 m (see Supplementary Note 3, Supplementary Table 2). The lower-energy cases, such as the 0.03 m wave height every 2 s, setting (H_s ~ 0.027 m, T_p ~ 1.93 s), produced disturbances slightly more energetic than a calm-ocean background. This is primarily due to their short period, which produces faster vertical accelerations than the long, slow undulations of background swell. The higher-energy conditions, such as the 0.075 m wave height every 2 s setting (H_s ~ 0.072 m, T_p ~ 2.05 s), generated considerably more dynamic forcing than calm surface motion, roughly comparable to the agitation associated with mild-to-moderate wind-driven chop in the ocean.

While the wave heights in these tests are small compared to open-ocean wind waves, the short periods deliver more frequent crest-trough cycles and thus more rapid oscillatory forcing. This makes them a useful means of qualitatively verifying device stability and functionality under periodic vertical disturbance. Importantly, even under the very high air temperatures

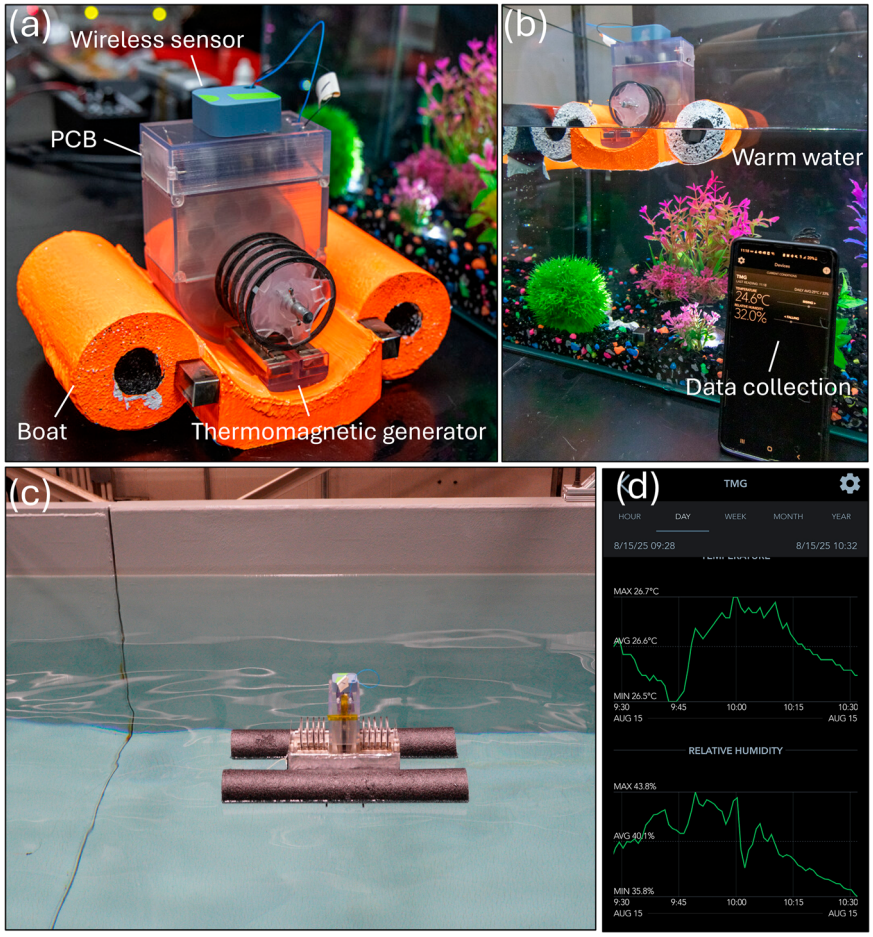

Fig. 10 | Deployable thermomagnetic boat used during the water and wave tank tests. a Assembled thermomagnetic generator with a mounted wireless sensor and PCB. Side-floating noodles are added to provide stability, and the structure is built from high-density ethylene-vinyl acetate (EVA) foam painted in safety orange for visibility and retrieval. (**b**) Proof-of-concept prototype deployment in a small aquarium with warm water, demonstrating continuous operation and real-time wireless data collection. (**c**) Large-scale deployment of the thermomagnetic generator boat in a water wave tank, validating stability and adaptability under realistic test conditions. (**d**) Wireless monitoring interface showing temperature and relative humidity data logged during operation of the device.

(~26 °C) present in the facility, the device continued to operate reliably. This test confirms that the device can operate without loss of function across the tested range, as shown in Fig. 10.

Case study: Kailua-Kona, Hawaii. The primary aim of this study is to assess the feasibility of deploying the thermomagnetic generator in thermal reservoirs such as the ocean for producing useful electricity from ultra-low temperature gradients. Offshore renewable energy facilities and activities such as ocean exploration require versatile, long-duration devices capable of continuous data transmission. For this technology to be effectively deployed and operated year-round, it requires nearly constant ocean and ambient temperatures and ideally wind conditions exceeding 1 m s^{-1}. The upper layer of the ocean (2–3 meters deep) has a heat capacity comparable to that of the entire atmosphere above it[42], which helps maintain more stable temperatures than those found on land. Additionally, wind-driven water movement enhances both cooling and heating HTCs due to the water mixing, improving overall heat transfer and creating optimal conditions for deployment.

Although several locations were considered, Kailua-Kona in Hawaii (Lat: 21.319°, Long: −157.668°) emerged as the most suitable site due to its consistently stable temperatures and year-round light winds. The presence of existing ocean thermal energy conversion plants and other renewable energy facilities in the area underscores this location's ideal conditions for such technologies.

Figure S8 (Supplementary note. 5) summarizes the average weather conditions at the selected study site. Notably, the temperature difference between the ocean and the ambient air remains nearly constant throughout the year. Coupled with consistent light winds exceeding 2 m s^{-1} at 10 meters above ground, which translates to higher than 1 m s^{-1} at 5 cm above the water surface, this ensures steady and reliable operation—even in scenarios with no temperature difference, according to the presented results. Under these conditions, more than 5 mW of power could be generated year-round, providing enough energy to power multiple wireless sensors for ocean research or offshore plants.

Scalability and design considerations. Our parametric evaluation identified wind speed as the most influential variable, as increased airflow enhances convective and evaporative cooling on the exposed ring surface. However, in environments where wind or low ambient temperatures are unavailable to assist cooling, design strategies that passively improve heat dissipation are critical. In this context, radial expansion, which increases the ring's side surface area, is expected to enhance thermal performance by facilitating greater convective and evaporative losses.

Gadolinium (Gd), as the most costly and scarce material component, must be used as efficiently as possible. Maximizing power output per unit mass is imperative. Combined with the inherent thermal limitations, this constraint shapes scalability. As the number of rotors increases, maintaining effective thermal transitions across the ring becomes more difficult. Experimental results (see Fig. 5) show that power density declines with additional rotors but plateaus beyond four. While modular configurations (e.g., two 10-rotor units) might not yield dramatically higher output than a single large system, they offer improved thermal control, better Gd utilization, and enhanced resilience: if one module fails, others remain operational.

Scaling by increasing rotor diameter is also possible, but manufacturing large, monolithic Gd rings is cost-prohibitive. Segmented rotors using smaller Gd pieces offer a more practical solution and are commonly used in actively heated and cooled systems[22–24]. However, segmentation has not yet

been validated in this passive configuration, and potential magnetic discontinuities may degrade performance. The heavy reliance on rare-earth thermomagnetic materials underscores the need for alternatives. Several transition-metal-based compounds and engineered composites have demonstrated promising thermomagnetic responses, offering pathways to reduce material costs and supply-chain vulnerability. Encouragingly, successful implementation of non-rare-earth thermomagnetic materials has been reported[20,25,43] opening opportunities for cost reductions and improving technology readiness.

Conclusions

A deployable concept for scavenging ultra-low temperature gradients—even zero in the presence of wind—has been studied and developed for powering IoT sensors and other low-voltage devices via the Curie effect. Unlike most previously researched thermomagnetic generators, this concept does not rely on forced convection for heating or cooling, thereby broadening its applications and simplifying the design.

- For most of the experiments presented in the study, ambient and hot water temperatures of 22.5 °C and 30 °C, respectively (a ΔT of 7.5 °C), were maintained, as this condition was shown to be optimal.
- The thermomagnetic generator Gd rings are immersed in a hot liquid reservoir. $\theta_{optimal}$ depends on the temperatures of the ambient (sink) and hot reservoir. These temperatures must be carefully balanced to ensure efficient heat transfer while minimizing drag.
- The thermomagnetic device can still produce power at immersion angles other than $\theta_{optimal}$; however, immersion angles lower than $\theta_{optimal}$ should be avoided to prevent unstable meniscus formation, characterized by intermittent wetting, which can hinder the performance due to the disrupted heating, interrupting the thermomagnetic cycle.
- As the air gap increases, higher angular speeds are required to achieve the same RMS voltage, indicating a performance decay characterized by lower power output and reductions in torque.
- The power output of the thermomagnetic generator increases with the number of rotors due to the volume of thermomagnetic material; however, the performance gain is not linear. A maximum power output of 0.62 mW and 2.05 mW was attained with 2 and 10 rotors, respectively. Power per rotor (power density) decreases quickly from 0.31 mW/rotor for 2 rotors to 0.205 mW/rotor for 10 rotors. This trend suggests that systems with fewer rotors may be more efficient than a single system with many rotors, although the overall cost would be higher.
- Contrary to initial expectations, the shaft plays a negligible role at the selected conditions and scale. Three different shafts, with substantially varying weights, yielded almost identical results, suggesting that choosing the sturdier and more stable alternative is preferable.
- The spacing of the rotors should ensure that the meniscus for each rotor remains independent, allowing for optimal performance while maximizing the freshness of the air between them. The positive effect of increasing the spacing between the rotors tends to saturate, ultimately leading to a decrease in power density per footprint.
- Wind impacts performance, confirming that the cooling process is the limiting factor for these systems. In the presence of wind at 1 m s^{-1}, power output increased threefold, rising from 2.13 mW to 6.7 mW. Additionally, power generation was achieved even with no temperature difference owing to enhanced evaporative cooling.
- It was successfully demonstrated that thermomagnetic generators can be self-sustainable and deployable in large water bodies by integrating them with a PCB equipped with supercapacitors. With just 21 minutes of charging, the thermomagnetic generator can power wireless sensors indefinitely without further assistance in remote and inaccessible areas.
- Multiple locations with ideal conditions for deploying the developed thermomagnetic device exist. Notably, Kailua-Kona in Hawaii, on average, provides an almost constant temperature difference and wind speeds exceeding 1 m s^{-1} at 0.05 meters above the ground year-round. At this location, the developed thermomagnetic generator could effectively power multiple IoT sensors for offshore activities such as ocean exploration, research, and renewable energy plant operations.
- Modular configurations improve thermal control, optimize Gd utilization, and enhance resilience, ensuring continued operation even if individual units fail.
- Segmentation and rare-earth-free thermomagnetic materials present promising avenues for scalable, cost-effective deployment and improved supply-chain stability.
- Other potential applications for this thermomagnetic device include geothermal renewable energy plants, solar facilities, and large data centers, just to name a few. The thermomagnetic material can be tailored to specific temperature ranges and environments based on requirements.

Future improvements for various types of applications will be pursued by exploring different heat sources and testing power production limits to enable the powering of larger sensors.

Methods

Experimental setup

The experimental setup consisted of Gd (purity 99.9%) ring-shaped rotors with an outer diameter of 50.5 mm and an inner diameter of 44.5 mm, and Ni-Cu-Ni-coated NdFeB (Grade N52) permanent magnets of size 2 inches × 1/2 inch × 1/4 inch, magnetized through the thickness. The chassis was manufactured using a 3D printer and polycarbonate resin that provided the necessary structural support for the components. We intentionally added a consistent number of Gd rings on each side of the axial flux generator, which is crucial to avoid frictional losses due to uneven load distribution. Considering the anticipated low angular speed and minimal bending loads, the use of bearings was intentionally limited to prevent additional frictional losses due to contamination, lubrication, and unevenness. This strategic approach aims to optimize the device's performance in scenarios with these specific mechanical characteristics. The Gd rings were deliberately exposed to the environment to harness potential wind effects, thereby enhancing convective heat transfer and reducing the cooling cycle time (i.e., increasing work output). Additionally, the axial flux generator housing was isolated from its surroundings to maintain dry conditions, as exposure to water poses a risk of potential damage to the generator. Overall, the deployable thermomagnetic generator prototype comprised 2–10 Gd rings, an axial flux generator, 2 pole pair permanent magnets (1 pole pair on each side), each with 10 small magnets. These components were mounted on a stainless-steel shaft supported by two bearings, providing structural alignment and rotational stability. The small permanent magnets were strategically positioned to enhance the magnetic flux density at the heated region of the Gd rings, as illustrated in Supplementary Figs. 3 and 4. For further information about the prototype components, refer to the Supplementary Methods section.

Axial flux generator

A dual-coreless rotor with a single-coreless stator axial flux permanent magnet generator was used to convert the magnetic work into useful electricity. Ten circular Ni-Cu-Ni-coated NdFeB (Grade N52) permanent magnets of 5/8 inch and 1/16 inch diameter, magnetized through the thickness, were used per rotor. The stator consisted of 10 coils, each with 600 turns of AWG 38 wire. The structure of the axial flux generator was manufactured using a 3D printer and polycarbonate. Additional information on the analysis and design of the axial flux generator is provided in the Supplementary Methods section, specifically Supplementary Figs. 5 and 6.

Experimentation

The voltage generated by the thermomagnetic generator was recorded using an NI 9207 cDAQ voltage and a current input module at a sampling rate of 25 hertz. The 12 W heaters were controlled using an NI 9472 cDAQ digital output module. The temperatures in the water and ambient air were

recorded using an NI 9213 temperature input module and calibrated T-type thermocouples from Omega. These were controlled using an NI cDAQ 9174 DAQ USB chassis and the LabVIEW software. The angular speed was measured every second using a non-contact-type optical digital tachometer DT-2100 from Checkline. A resistance substitute box was used to vary the resistance during the experiments.

Resource availability

Lead contact. Further information and requests for resources should be directed to and will be fulfilled by the lead contact, Ravi A. Kishore (ravi.kishore@nrel.gov).

Materials availability. The datasets generated during and/or analyzed during the current study are available from the corresponding author on reasonable request.

Received: 5 May 2025; Accepted: 27 October 2025;
Published online: 27 November 2025

References

1. Forman, C., Muritala, I. K., Pardemann, R. & Meyer, B. Estimating the global waste heat potential. *Renew. Sustain. Energy Rev.* **57**, 1568–1579 (2016).
2. Van de Bor, D. M., Ferreira, C. A. I. & Kiss, A. A. Low grade waste heat recovery using heat pumps and power cycles. *Energy* **89**, 864–873 (2015).
3. Bian, Q. Waste heat: the dominating root cause of current global warming. *Environ. Syst. Res.* **9**, 1–11 (2020).
4. Firth, A., Zhang, B. & Yang, A. Quantification of global waste heat and its environmental effects. *Appl. energy* **235**, 1314–1334 (2019).
5. Zevenhoven, R. & Beyene, A. The relative contribution of waste heat from power plants to global warming. *Energy* **36**, 3754–3762 (2011).
6. Ja'fari, M., Khan, M. I., Al-Ghamdi, S. G., Jaworski, A. J. & Asfand, F. Waste heat recovery in iron and steel industry using organic Rankine cycles. *Chem. Eng. J.* **477**, 146925 (2023).
7. Bin Wan Ramli, W. R., Pesyridis, A., Gohil, D. & Alshammari, F. Organic rankine cycle waste heat recovery for passenger hybrid electric vehicles. *Energies* **13**, 4532 (2020).
8. DeLovato, N., Sundarnath, K., Cvijovic, L., Kota, K. & Kuravi, S. A review of heat recovery applications for solar and geothermal power plants. *Renew. Sustain. Energy Rev.* **114**, 109329 (2019).
9. Modi, A. & Haglind, F. Performance analysis of a Kalina cycle for a central receiver solar thermal power plant with direct steam generation. *Appl. Therm. Eng.* **65**, 201–208 (2014).
10. Liu, Z. et al. Demonstration of ultrahigh thermoelectric efficiency of~ 7.3% in Mg3Sb2/MgAgSb module for low-temperature energy harvesting. *Joule* **5**, 1196–1208 (2021).
11. Nader, W. B., Chamoun, J. & Dumand, C. Thermoacoustic engine as waste heat recovery system on extended range hybrid electric vehicles. *Energy Convers. Manag.* **215**, 112912 (2020).
12. Zhang, Y. et al. Thermal energy harvesting using pyroelectric-electrochemical coupling in ferroelectric materials. *Joule* **4**, 301–309 (2020).
13. Kennedy, B. R. & Rotjan, R. D. Mind the gap: comparing exploration effort with global biodiversity patterns and climate projections to determine ocean areas with greatest exploration needs. *Front. Mar. Sci.* **10**, 1219799 (2023).
14. LiVecchi, A. et al. Powering the blue economy; exploring opportunities for marine renewable energy in maritime markets. (U.S. Department of Energy, Office of Energy Efficiency and Renewable Energy., Washington, D.C., 2019).
15. Venkatesan, R., Tandon, A., Sengupta, D. & Navaneeth, K. Recent trends in ocean observations. In *Observing the Oceans in Real Time*, 3–13 (2018).
16. Ayers, J. M. & Richter, K. In *OCEANS 2016 MTS/IEEE Monterey*. 1–6 (IEEE).
17. Tesla, N. (Google Patents, 1889).
18. Murakami, K. & Nemoto, M. Some experiments and considerations on the behavior of thermomagnetic motors. *IEEE Trans. Magn.* **8**, 387–389 (1972).
19. Takahashi, Y., Matsuzawa, T. & Nishikawa, M. Fundamental performance of the disc-type thermomagnetic engine. *Electr. Eng. Jpn.* **148**, 26–33 (2004).
20. Kishore, R. A. & Priya, S. Low-grade waste heat recovery using the reverse magnetocaloric effect. *Sustain. Energy Fuels* **1**, 1899–1908 (2017).
21. Kishore, R. A. & Priya, S. A review on design and performance of thermomagnetic devices. *Renew. Sustain. Energy Rev.* **81**, 33–44 (2018).
22. Andreevskii, K. N., Mandzhavidze, A. G., Margvelashvili, I. G. & Sobolevskaya, S. V. Investigation of the thermodynamic and physical characteristics of a thermomagnetic engine with a gadolinium working element. *Tech. Phys.* **43**, 1115–1118 (1998).
23. Ahmed, R. et al. Optimization of a cylindrical thermomagnetic engine for power generation from low-temperature heat sources. *Int. J. Energy Res.* **45**, 8606–8619 (2021).
24. Mehmood, M. U. et al. Design and operation of a thermomagnetic engine for the exploitation of low-grade thermal energy. *Int. J. Energy Res.* **45**, 15298–15311 (2021).
25. Hey, J., Repaka, M., Li, T. & Tan, J. L. Design optimization of a rotary thermomagnetic motor for more efficient heat energy harvesting. *Energies* **15**, 6334 (2022).
26. Esposito, G., Hey, J. & Fasano, M. In *ASTFE Digital Library*. (Begel House Inc.).
27. Kishore, R. A. et al. Energy scavenging from ultra-low temperature gradients. *Energy Environ. Sci.* **12**, 1008–1018 (2019).
28. Imam, S. A., Choudhary, A. & Sachan, V. K. In *International Conference on Soft Computing Techniques and Implementations (ICSCTI)*. 181–187 (IEEE) (2015).
29. Yang, J., Liu, Q., Ding, F. & Ding, R. A spherical temperature sensor array design for near-surface atmospheric temperature studies. *J. Atmos. Ocean. Technol.* **37**, 1497–1506 (2020).
30. Graham, C. D. Jr. Magnetic behavior of gadolinium near the Curie point. *J. Appl. Phys.* **36**, 1135–1136 (1965).
31. Liu, X. et al. Significant optimization of active thermomagnetic generator for low-grade waste heat recovery. *Appl. Therm. Eng.* **221**, 119827 (2023).
32. Miao, L. et al. Comfortable wearable thermoelectric generator with high output power. *Nat. Commun.* **15**, 8516 (2024).
33. Fan, W. et al. High-performance stretchable thermoelectric generator for self-powered wearable electronics. *Adv. Sci.* **10**, 2206397 (2023).
34. Wei, H., Zhang, J., Han, Y. & Xu, D. Soft-covered wearable thermoelectric device for body heat harvesting and on-skin cooling. *Appl. Energy* **326**, 119941 (2022).
35. Hong, S. et al. Wearable thermoelectrics for personalized thermoregulation. *Sci. Adv.* **5**, eaaw0536 (2019).
36. Hu, K. et al. Optimized thermal design for excellent wearable thermoelectric generator. *J. Mater. Chem. A* **10**, 24985–24994 (2022).
37. Li, X. et al. Breeze-driven triboelectric nanogenerator for wind energy harvesting and application in smart agriculture. *Appl. Energy* **306**, 117977 (2022).
38. Dang, H. et al. Triboelectric-electromagnetic hybrid generator with the inertia-driven conversion mechanism for wind energy harvesting and scale warning. *Mater. Today Energy* **29**, 101136 (2022).
39. Wang, Z. et al. Hybridized energy harvesting device based on high-performance triboelectric nanogenerator for smart agriculture applications. *Nano Energy* **102**, 107681 (2022).

40. An, J., Wang, Z. M., Jiang, T., Liang, X. & Wang, Z. L. Whirling-folded triboelectric nanogenerator with high average power for water wave energy harvesting. *Adv. Funct. Mater.* **29**, 1904867 (2019).
41. Zhang, C. et al. Passive wireless marine Internet-of-Things buoy based on hybrid nanogenerator with omnidirectional water-wave energy harvesting. *Nano Energy* **138**, 110809 (2025).
42. Soloviev, A. & Lukas, R. *The near-surface layer of the ocean: structure, dynamics and applications*. Vol. 48, Springer Science & Business Media (2013).
43. Huang, B. *Design and Analysis of Magnetocaloric Devices for Cooling Heating and Waste Heat Recovery*. https://repository.tudelft.nl/record/uuid:1027d16b-3082-438d-8d9c-ef2949c11211 (2024).

Acknowledgements

This work was authored by NREL for the U.S. Department of Energy (DOE), operated under Contract No. DE-AC36-08GO28308. Funding provided by the U.S. Department of Energy Office of Energy Efficiency and Renewable Energy Water Power Technologies Office. The views expressed in the article do not necessarily represent the views of the DOE or the U.S. Government. The U.S. Government retains, and the publisher, by accepting the article for publication, acknowledges that the U.S. Government retains a non-exclusive, paid-up, irrevocable, worldwide license to publish or reproduce the published form of this work, or allow others to do so, for U.S. Government purposes.

Author contributions

R.A.K. conceived the idea and carried out the modeling and simulations. E.M.R. fabricated the device and performed experiments. T.P. supported the experiments and designed the electronic circuit for energy storage. R.A.K. and E.M.R. conducted data analysis and discussions. R.A.K. supervised the research. All authors contributed to the writing and revision of the manuscript.

Competing interests

A U.S. provisional patent application entitled “Thermomagnetic Generator for Marine Thermal Energy Harvesting” (Application No. 63/754,371), authored by Ravi Kishore and Erick Moreno Resendiz, has been filed with the United States Patent and Trademark Office.

Additional information

Supplementary information The online version contains supplementary material available at https://doi.org/10.1038/s44172-025-00542-y.

Correspondence and requests for materials should be addressed to Ravi Anant Kishore.

Peer review information *Communications Engineering* thanks Jiaxing Xu and the other, anonymous, reviewer(s) for their contribution to the peer review of this work. A peer review file is available. Primary Handling Editors: Wenjie Wang and Rosamund Daw.